A Particle Immersed Boundary Method for Flow-Structure Interactions involving Complex Geometries

S. E. Hieber and P. Koumoutsakos
Institute of Computational Science, ETH Zurich
hiebers@inf.ethz.ch, petros@inf.ethz.ch

January 24, 2007

Abstract

We present a novel particle Immersed Boundary Method to enforce no-slip boundary conditions on complex geometries. A forcing term appearing in the momentum equation is evaluated on the boundary points such that the no-slip boundary condition is fulfilled on the boundary. The method applied to an isothermal compressible fluid is capable of approximating the flow of incompressible medium at a Mach Number of 0.05. The efficiency and accuracy of the method is demonstrated in several benchmark problems in two and three dimensions involving flow past a cylinder/sphere. The particle Immersed Boundary Method is shown to be well suited for the simulations of anguilliform swimming.

1 Introduction

Biofluid dynamics is characterized by the interaction of elastic incompressible tissue with viscous incompressible fluid. In some cases the elastic tissue is active, like muscle, which means that it can act a source of mechanical energy. The Immersed Boundary Method is both a mathematical formulation and a computational method for the biofluid dynamic problem. In the immersed boundary formulation, the equations of fluid dynamics are used in an unconventional way, to describe not only the fluid but also the immersed tissue with which it interacts. In the computational scheme motivated by this formulation, the fluid equations are solved on a fixed (Eulerian) cubic lattice, where elastic forces are computed from a Lagrangian representation of the immersed elastic tissue. The material points of the tissue move freely through the cubic lattice of the fluid computation. The two components of this Eulerian/Lagrangian scheme are linked by a smoothed version of the Dirac delta function, which is used to apply elastic forces to the fluid, and to interpolate the fluid velocity at the representative material points of the elastic tissue. This methodology has been

applied to the heart and its valves by Peskin [23] who introduced this method within this context.

Fadlun and Verzicco *et al.* [9] proposed an immersed boundary method for finite-difference methods where the velocity of fluid cells close the complex boundary is interpolated linearly between the boundary and the neighboring fluid cell. This method leads to second order accuracy and requires a accurate distance-information to the boundary at the all neighboring fluid cells. Kim [19] presented a similar approach for finite-volume methods combined with a mass source to increase the accuracy.

These approaches, however, are limited to Eulerian methods for incompressible flows. We present a novel particle Immersed Boundary method (pIBM) that is applicable to Lagrangian particle methods, such as smoothed particle hydrodynamics. The geometry of the body is described by Lagrangian points. A forcing term is evaluated on the boundary points such that the no-slip boundary condition on the body is fulfilled. The extrapolation of the forcing term onto the neighboring particles involves high-order B-Splines kernel.

We demonstrate the performance of the pIBM on channel flow, flow past a circular cylinder and sphere. We compare the characteristic numbers of the flow for various Reynolds numbers with experimental and numerical results presented in the literature.

2 Governing Equations

A system of differential equations govern the motion of a viscous, compressible medium. The fundamental system describes the conservation of mass and momentum. The conservation equations for a fluid are

$$\frac{D\rho}{Dt} = -\rho\nabla\cdot\mathbf{u} \tag{1}$$

$$\rho\frac{D\mathbf{u}}{Dt} = -\nabla p + \nabla.\tau \tag{2}$$

$$\tau_{ij} = \mu\left(\frac{\partial u_i}{\partial x_j} + \frac{\partial u_j}{\partial x_i} - \frac{2}{3}\delta_{ij}\frac{\partial u_k}{\partial x_k}\right) \tag{3}$$

where $\frac{D\diamond}{Dt} = \frac{\partial\diamond}{\partial t} + (u\cdot\nabla)(\diamond)$ denotes the material derivative, ρ denotes the density, u the velocity, p the pressure, τ the shear stress tensor with the elements τ_{ij} and μ the viscosity. x_i are the components of the position, u_i the components of the velocity where Einstein's summation convention must be taken into account.

The system of differential equations Eq.(1)-(3) is closed with the equation of state for an ideal gas

$$p = \rho RT \tag{4}$$

where R is the specific gas constant and T the temperature. We assume the temperature $T = T_0$ to be constant in space and time. The reference density is ρ_0.

The initial condition is described by a density and a velocity field. The immersed boundary is governed by a no-slip boundary condition. The inflow boundary involves a prescribed inlet velocity and a homogenous Neumann boundary condition for the pressure. At the outlet, we consider a prescribed outlet pressure and a homogenous Neumann boundary condition for the velocity.

2.1 Definitions of Characteristic Numbers

The Reynolds number of the flow is defined as

$$Re = \frac{\rho U d}{\mu}, \tag{5}$$

where ρ is the characteristic density of fluid, U the characteristic velocity, μ the dynamic viscosity. The characteristic length d is equal to the channel width or the cylinder/sphere diameter depending on the considered problem.

The Mach number M is the ratio of the characteristic velocity U to the speed of sound c_0

$$M = \frac{U}{c_0} = \frac{U}{\sqrt{RT_0}} \tag{6}$$

The drag coefficient is an important characteristic that is commonly used to validate flow simulations. It is defined as

$$C_d = \frac{F_D}{0.5\rho U^2 A}, \tag{7}$$

where F_D, the drag force, is force acting on the body parallel to the main stream direction and A the reference area. Similar to the drag coefficient the lift coefficient is defined as

$$C_L = \frac{F_L}{0.5\rho U^2 A}, \tag{8}$$

where F_L, the lift force, is the force acting perpendicular to the main stream.

The Strouhal number is defined as the dimensionless frequency of the shedding vortices

$$St = \frac{f d}{U}, \tag{9}$$

where f is the vortex shedding frequency. This frequency can be obtained using the Fast Fourier Transform of the lift coefficient.

3 Particle Presentation of Immersed Boundaries

3.1 Function and Gradient Approximations Using Particles

In the context of particle methods [5, 11, 3] a smooth approximation of a function $\Phi(\mathbf{x})$ can be constructed by using a mollification kernel $\zeta_\epsilon(\mathbf{x})$:

$$\Phi_\epsilon(\mathbf{x}) \;=\; \Phi \star \zeta_\epsilon \;=\; \int \Phi(\mathbf{y})\, \zeta_\epsilon(\mathbf{x}-\mathbf{y})\, d\mathbf{y} \tag{10}$$

where ϵ denotes a characteristic length of the kernel.

The kernel is said to be of order r when the following moment conditions [5] are satisfied:

$$\int \zeta_\epsilon(\mathbf{x}) d\mathbf{x} = 1, \tag{11}$$

$$\int \mathbf{x}^i \zeta_\epsilon(\mathbf{x}) d\mathbf{x} = 0 \quad \text{if } |i| \leq r-1, \tag{12}$$

$$\int |\mathbf{x}|^r \zeta_\epsilon(\mathbf{x}) d\mathbf{x} \leq \infty \tag{13}$$

This mollified approximation $\Phi_\epsilon(\mathbf{x})$ can be discretised using the particle locations as quadrature points and a particle approximation of the regularized function is

$$\Phi^h_\epsilon(\mathbf{x}) \;=\; \Phi^h \star \zeta_\epsilon \;=\; \sum_{p=1}^{N} v_p \Phi_p \zeta_\epsilon(\mathbf{x}-\mathbf{x}_p) \tag{14}$$

where $\mathbf{x}_p$, and v_p denote the position and volume of the p-th particle, and $\Phi_p = \Phi(\mathbf{x}_p)$ the value at the $p = 1, \cdots, N$ particle locations.

As discussed in [5] the error introduced by the quadrature of the mollified approximation of Φ can be distinguished in two parts as

$$\Phi \;-\; \Phi^h_\epsilon \;=\; (\Phi \;-\; \Phi \star \zeta_\epsilon) \;+\; (\Phi \;-\; \Phi^h) \star \zeta_\epsilon \tag{15}$$

The first term in Eq. (15) denotes the mollification error that can be controlled by appropriately selecting the kernel properties. The second term denotes the quadrature error due to the approximation of the integral on the particle locations. The overall accuracy of the method [5] results in

$$\|\Phi - \Phi^h_\epsilon\|_{0,p} \;\leq\; \|\Phi - \Phi_\epsilon\|_{0,p} \;+\; \|\Phi_\epsilon - \Phi^h_\epsilon\|_{0,p} \sim\; \mathcal{O}(\epsilon^r) \;+\; \mathcal{O}\left(\frac{h^m}{\epsilon^m}\right) \tag{16}$$

where $\|(.)\|_{0,p} = \left(\int (.)^p \, d\mathbf{x}\right)^{1/p}$ and r denotes the order of the first non-vanshing moment of the kernel ζ_ϵ [5]. For equidistant particle locations $m = \infty$ and for positive kernels such as the Gaussian, $r = 2$. Here for ζ_ϵ a quartic spline kernel

with second order of accuracy is implemented:

$$\zeta_\epsilon(\mathbf{x}) = n_d \bar{\zeta_\epsilon} = n_d \begin{cases} \frac{s^4}{4} - \frac{5s^2}{8} + \frac{115}{192} & 0 \le s < \frac{1}{2}, \qquad s = \frac{|\mathbf{x}|}{\epsilon}, \\ -\frac{s^4}{6} + \frac{5s^3}{6} - \frac{5s^2}{4} + \frac{5s}{24} + \frac{55}{96} & \frac{1}{2} \le s < \frac{3}{2}, \\ \frac{(2.5-s)^4}{24} & \frac{3}{2} \le s < \frac{5}{2}, \\ 0 & s \ge \frac{5}{2}. \end{cases} \tag{17}$$

The normalization value n_d depends on the dimension of the problem and is computed as:

$$n_d = \frac{1}{\sum_j v_j \bar{\zeta_\epsilon}(\mathbf{x} - \mathbf{x}_j)} \tag{18}$$

ensuring the property of *partition of unity* for the particles. Kernels of arbitrary order [1] are possible by giving up the positivity of the kernel function.

The error estimates reveal a very important fact for smooth particle approximations. In order to obtain accurate approximations of the *smooth particles must overlap*. Note that the moment conditions expressed by the integrals of the mollifier functions are not often well represented in the case of discrete particle sets. These moment conditions can be ensured by appropriate normalisations [5].

3.2 Remeshing

A key aspect of the present method involves the use of a remeshing procedure. In smooth particle methods, as discussed earlier, particles must overlap at all times in order to guarantee the convergence of the method [6]. As it is shown in [4] remeshing is equivalent to a regularisation of the particle description of the advected quantities.

In this work remeshing is employed in order to regularize the distorted particle locations and to redistribute particle quantities accordingly onto a uniform set of particles with the spacing h. The redistribution of particle quantities is achieved using the 3rd order $M'4$ kernel [20] which in one dimension is expressed as:

$$M_4^{'}(x,h) = \begin{cases} 1 - \frac{5s^2}{2} + \frac{3s^3}{2} & 0 \le s < 1, \qquad s = \frac{|x|}{h} \\ \frac{(1-s)(2-s)^2}{2} & 1 \le s < 2, \\ 0 & s \ge 2. \end{cases} . \tag{19}$$

In higher dimensions the interpolation formulas are tensorial products of their one-dimensional counterparts. Remeshing at complex boundaries requires a normalization scheme of the remeshed quantities. The normalization scheme is similar to the normalization that ensures the partition of unity (Eq. (18)).

$$\Phi_{j,new} = \frac{V_{new}}{\sum_{i=1}^{N_{old}} V_{old} M'4(|x_i - x_j|, h)} \sum_{i=1}^{N_{old}} \Phi_{i,old} M'4(|x_i - x_j|, h) \tag{20}$$

where $V_{new} = h^3$ is the volume of the new particle. We redistribute the extensive properties of the particle that need to be conserved, namely mass and momentum.

3.2.1 Particle Derivative Approximations

Particle approximations of the derivative operators can be constructed through their integral approximations. This can be achieved by taking the derivatives of Eq.(10) as convolution and derivative operators commute in unbounded or periodic domains. This approximation is popular in particle methods such as Smooth Particle Hydrodynamics (SPH) [21] where derivatives of a field quantity Φ on a particle p are approximated in a conservative form as:

$$\left\langle \frac{\partial}{\partial x_i}\Phi \right\rangle_p = \sum_q v_q \left(\Phi_q - \Phi_p\right) \frac{\partial}{\partial x_i}\zeta_\epsilon(\mathbf{x}_p - \mathbf{x}_q), \tag{21}$$

$$\left\langle \frac{\partial}{\partial x_i x_j}\Phi \right\rangle_p = \sum_q v_q \left(\Phi_q - \Phi_p\right) \frac{\partial}{\partial x_i x_j}\zeta_\epsilon(\mathbf{x}_p - \mathbf{x}_q), \tag{22}$$

where v_q is the volume of particle q. The normalization values $n_{d,1}, n_{d,2}$ of $\frac{\partial}{\partial x_i}\zeta_\epsilon(\mathbf{x}) = n_{d,1}\frac{\partial}{\partial x_i}\bar{\zeta}_\epsilon(\mathbf{x})$ and $\frac{\partial}{\partial x_i x_j}\zeta_\epsilon(\mathbf{x}) = n_{d,2}\frac{\partial}{\partial x_i x_j}\bar{\zeta}_\epsilon(\mathbf{x})$ are chosen such that the corresponding non-zero moment condition [8] is statisfied. The kernel of Eq. (17) has its first three derivatives continuous allowing a smooth approximation of the spatial derivatives of $\Phi(\mathbf{x})$. The computation of the right hand side of the ODEs employs these formulas for the computation of derivatives as defined in Eq.(1) - (3). An alternative formulation involves the development of integral operators that are equivalent to differential operators [8] as they were first introduced for the integral approximation of the Laplacian [7] in the diffusion equation.

3.3 Particle Immersed Boundary Method (pIBM)

In pIBM (Fig.1), a forcing term f is added to the momentum equation (Eq.(2)) such that the no-slip condition is satisfied on the boundary.

$$\rho\frac{Du}{Dt} = -\nabla p + \nabla.\tau + f \tag{23}$$

We approximate the material derivative by a differential quotient:

$$\rho_i\frac{u_{i+1} - u_i}{\Delta t} = -\nabla p_i + \nabla.\tau_i + f_i \tag{24}$$

Solving for f_i and assuming we reach the desired velocity within this time step ($u_{i+1} = u_{desired}$) yields

$$f_i = \rho_i\frac{u_{desired} - u_i}{\Delta t} - (-\nabla p_i + \nabla.\tau_i) \tag{25}$$

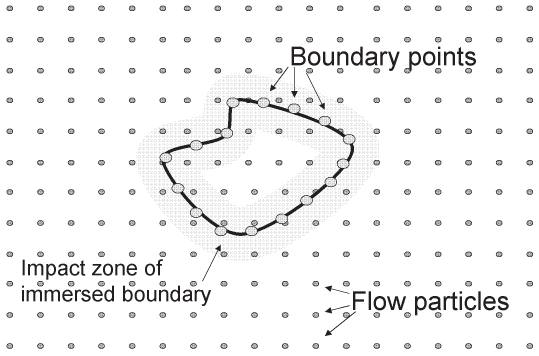

Figure 1: Particle Immersed Boundary Method. The immersed boundary is discretized using boundary points that can only i flow particles within the kernel support.

Note that the forcing term f acts locally on the boundaries where a no-slip condition is imposed and the velocity $u_{desired}$ is known. The boundary is described by boundary points associated with a surface area. We employ a Kernel based on B-Splines for a dirac delta approximation of the forcing term f. We use particle-mesh, mesh-particle interpolation schemes for performance reasons.

Our implementation involves the separation of the forcing term into two parts:

$$f_i = \rho_i(f_{ip} + f_i b) \tag{26}$$

$$f_{ip} = \frac{-u_i}{\Delta t} - \frac{1}{\rho_i}\left(-\nabla p_i + \nabla.\tau_i\right) \tag{27}$$

$$f_{ib} = \frac{u_{desired}}{\Delta t} \tag{28}$$

The pIBM consists the following steps:

1. Evaluation of the first part of the forcing term f_{ip} on the particle
2. Interpolation of f_{ip} from the particles onto the boundary points via mesh.
3. Evaluate forcing term f_i on the boundary points by adding f_{ib}
4. Interpolation of forcing term f from the boundary points to the particles via mesh.
5. Evolving particles according to the governing equations including forcing term f

3.4 Particle Equations

The particle position $\mathbf{x}_p$, mass m_p, volume v_p, and velocity component $\mathbf{u}_{i,p}$ evolve by the following system of ordinary differential equations derived from Eq.(1),(2) and (3)

$$\begin{aligned}
\frac{d\mathbf{x}_p}{dt} &= \mathbf{u}_p \\
\frac{dm_p}{dt} &= 0 \\
\frac{dv_p}{dt} &= \langle \nabla \cdot \mathbf{u} \rangle_p v_p \\
\frac{d\mathbf{u}_{i,p}}{dt} &= \frac{v_p}{m_p} \left(-\langle \frac{\partial p}{\partial x_i} \rangle_p + \langle \frac{\partial \tau_{ij}}{\partial x_j} \rangle_p \right) + f_{i,p}
\end{aligned} \tag{29}$$

where $\langle \diamond \rangle_p$ denotes the derivative approximation on a particle p (cf. Eq. (21)) and

$$\langle \frac{\partial \tau_{ij}}{\partial x_j} \rangle_p = \mu \left(\langle \frac{\partial^2 u_i}{\partial x_k^2} \rangle_p + \frac{1}{3} \langle \frac{\partial^2 u_l}{\partial x_i \partial x_l} \rangle_p \right) \tag{30}$$

$$p_p = \frac{m_p}{v_p} R T_0 \tag{31}$$

In the present study, the Laplacian approximation $\langle \frac{\partial^2 u_i}{\partial x_k^2} \rangle_p$ is evaluated using the particle strength exchange approach [7] to increase the stability of the simulations.

$$\langle \frac{\partial^2 u_i}{\partial x_k^2} \rangle_p = \sum_p v_p \left(\Phi_p - \Phi_q \right) \nabla^2 \zeta_\epsilon (\mathbf{x}_q - \mathbf{x}_p) \tag{32}$$

$$\zeta_\epsilon = \frac{15}{\epsilon^{-3} \pi} \frac{1}{|x|^{10} + 1} \tag{33}$$

The second order kernel ζ_ϵ was successfully applied in diffusion simulations involving complex geometries [27].

The interface between the body and the fluid is captured using the Particle Level Set Method [14, 13]. The level set function represents the signed distance function to the interface. The particles carry the level set information as a scalar attribute Φ_p that remains constant during the time integration:

$$\frac{d\Phi_p}{dt} = 0 \tag{34}$$

We reinitialize the level set value after every remeshing to maintain the signed distance property. The exact knowledge of the body shape allows the reinitialization of the level set function with its analytical value.

The inlet and outlet boundary conditions are imposed by using image particles that have similar physical properties as the flow particles. The boundary particles interact with the flow particles such that the boundary conditions are satisfied. The no-slip boundary condition on the body surface is handled by the proposed particle Immersed Boundary Method.

4 Results

We demonstrate the performance of the presented Immersed Boundary Method on several test problems and compare with results presented in the literature. We consider the Poiseuille flow, flow past a cylinder and sphere and an anguilliform swimming. The comparison is based on several non-dimensional characteristic flow numbers.

4.1 Poiseuille flow

A classic, and simple, problem in viscous, laminar flow involves the steady-state velocity and pressure distribution for a fluid moving laterally between two plates. The flow is driven by a pressure gradient in the direction of the flow, and is retarded by viscous drag along both plates, such that these forces are in balance. The simulation domain was considered to be a unit square with periodic boundary condition at the inlet/outlet boundary (x=0, x=1) and no-slip conditions at the plates (y=0, y=1). We consider a fluid density with an initial density of $\rho = \rho_0 = 1$ at a Reynolds number of $Re = 100$ and a Mach number of $M = 0.5$. The fluid is initially at rest and accelerated by an artifical constant pressure gradient of 0.001. The time integration scheme is a Runge Kutta scheme of 2nd order with a time step of $\delta t = 0.0005$ in all cases. For the error analysis the maximal difference in the velocity profile to the analytical solution is evaluated when the profile becomes stationary at time $T = 70$. The error normalized by the maximal velocity is shown in Fig. 2. The error analysis shows the flow simulations are second order accurate in space.

4.2 Flow past a cylinder

We present the simulation of flow past a cylinder for various Reynolds numbers to demonstrate the performance of the particle Immersed Boundary Method and compare with previous results presented in the literature. The flow past a circular cylinder is associated with various instabilities. These instabilities involve the wake, the separated shear layer and the boundary layer depending on the Reynolds number. Up to $Re \approx 47$, the flow is steady with two symmetric vortices on each side of the wake centre line. The first wake instability, manifestation of a Hopf bifurcation, occurs at $Re \approx 47$. For $Re > 47$, although remaining laminar, the flow becomes unsteady and asymmetric. Von Karman vortex shedding is observed for slightly larger Re. At $Re \approx 190$, three-dimensional instabilities, such as formation of vortex loops, deformation of primary vortices and stream

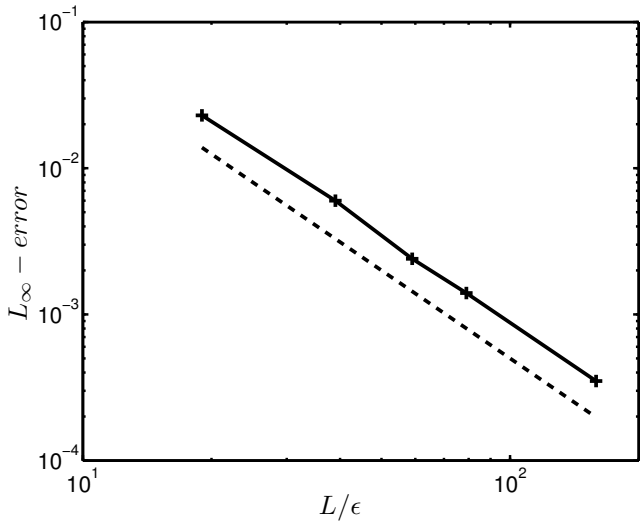

Figure 2: Poiseuille flow: $L_\infty-$ error velocity of the particle Immersed Boundary Method (pIBM) compared to second order scaling (dashed line)

wise and span wise vortices appear in wake. The wake flow undergoes a series of complex three-dimensional instabilities, making the flow eventually turbulent. Beyond a certain critical Re, the shear layer separating from the upper and lower surface of the cylinder starts becoming unstable via the Kelvin-Helmholtz mode of instability. The transition point, beyond which the separated layer becomes unstable, moves upstream with the increase of the Reynolds number. At $Re \approx 2 \cdot 10^5$, the boundary layer on the cylinder surface undergoes a transition from laminar to turbulent.

We use the Runge Kutta 4th order scheme for time integration with constant time step of $\Delta t = 0.005$. The domain size is set to $15d \times 30d$ where d is the diameter of the cylinder. The Mach number M is 0.05 The solution is remeshed after every time step. The fluid is initially at rest and accelerated by a small artificial force until the desired inlet velocity is reached to avoid the development of pressure wave at the boundary.

Fig. 3 and Fig. 4 shows the vorticity field at $Re = 100$ and $Re = 1000$ respectively. The instability is trigged by a pertubation of the inlet velocity in lateral direction as described by Plouhams [25]. The vorticity field match well with the Finite Element solutions presented by Singh *et al.* [29] in both cases. The simulations require a particle spacing of $h = 0.078d$ for $Re = 100$ and $h = 0.052d$ for $Re = 1000$.

Fig. 5 shows the variation of the drag coefficient with the Reynolds number. The simulation results of the pIBM are compared with experimental results and computations considering incompressible flow. It is observed that the values from present computations match well the experiments for $Re < 200$. In

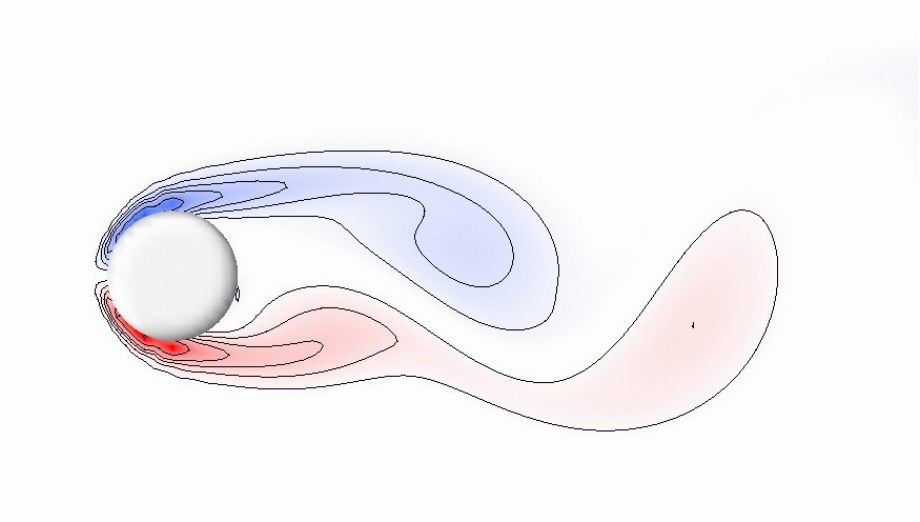

Figure 3: Flow past a cylinder at $Re = 100$. Contour levels of the vorticity contours at ($\pm 20, \pm 15, \pm 10, \pm 7.5, \pm 5, \pm 2.5$)

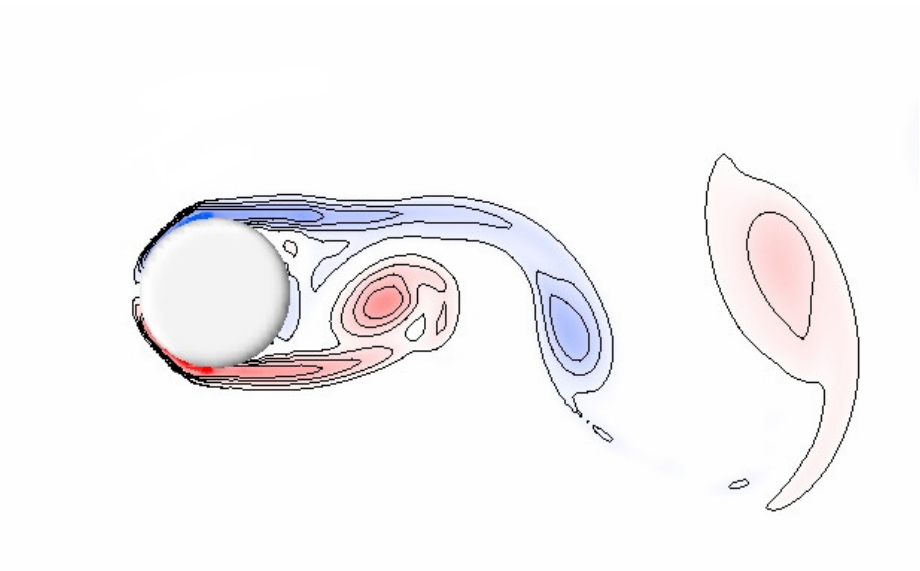

Figure 4: Flow past a cylinder at $Re = 1000$. Contour levels of the vorticity contours at ($\pm 20, \pm 15, \pm 10, \pm 5$)

particular, Table 1 shows the excellent agreement to experiments and previous simulation results with respects to drag coefficient and Strouhal number.

Beyond $Re = 180$ the wake flow undergoes three-dimensional transitional instabilities. Therefore, for $Re > 200$ the drag coefficient and the Strouhal number are overpredicted by two-dimensional computations.

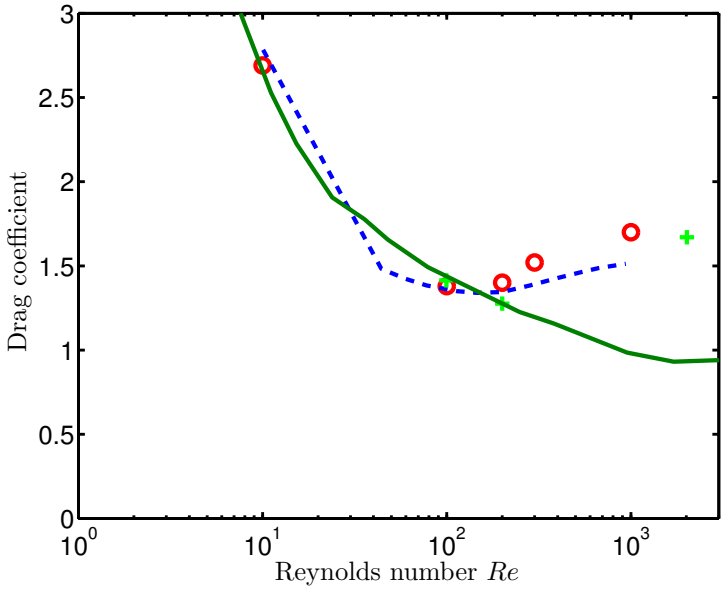

Figure 5: Flow past a cylinder: Time averaged drag coefficient of pIBM (circles) versus Reynolds number in comparison with experimental data (solid line, taken from [26]) , a Spectral Method (dashed line, taken from [29]) and a FEM solution (crosses) [29]

Table 1: Flow past a cylinder: Comparison with previous simulations and experiments

$Re = 100, D = 0.2$	Drag coefficient	Strouhal number
pIBM	1.38	0.162
Henderson [12]	1.35	-
Park *et al.* [22]	1.33	0.165
Silva *et al.* IBM [28]	1.39	0.162
Singh *et al.* FEM [29]	1.41	0.164
Kim *et al.* FV IBM [19]	1.33	0.165
Wieselberger (Exp.) taken from [26]	1.45	-
Williamson (Exp.) [30]	-	0.165

Fig. 6 shows the pressure coefficient of the time averaged flow along the cylinder surface for $Re = 100$ compared to the result of Park *et al.* [22]. The angle θ is measured from the stagnation point of the incoming flow towards the outlet. The pressure coefficient C_p agrees well with the results of Park *et al.* [22]. The pressure field tends to reveal noise at the angle $10° < \theta < 50°$ due to unresolved pressure waves in the compressible fluid.

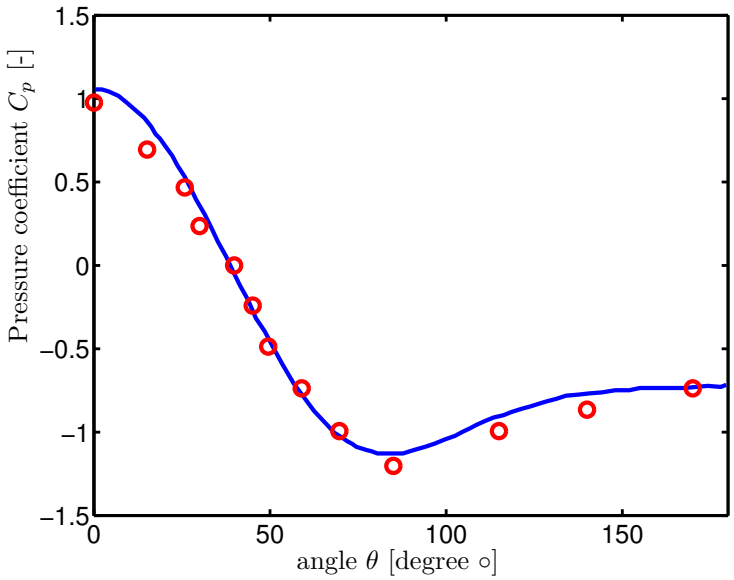

Figure 6: Flow past a cylinder at $Re = 100$: Pressure coefficient C_p (circle) versus angle in comparison with the solution of Park [22] (solid line)

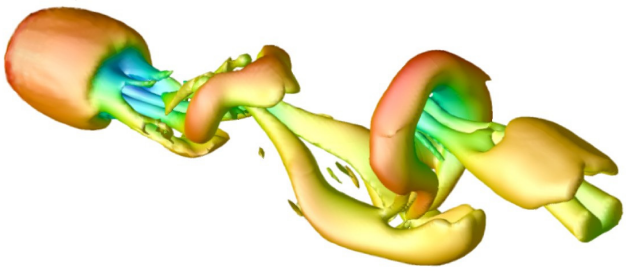

Figure 7: Flow past a sphere at $Re = 300$. The vortices behind the sphere are visualized using the λ_2 method [15]. The color represent the local flow velocity.

4.3 Flow past a sphere

Wakes of incompressible fluid behind spheres are observed to be steady for Reynolds numbers below 270. Above this limit vortices break off and are periodically released to form vortex loops that are connected like in a chain. We consider the flow past a sphere at $M = 0.1$ and $Re = 100$ and $Re = 300$. Table 2) shows that the drag and lift coefficient of the pIBM compare well with the simulation results considering incompressible fluid. The domain size is $10d \times 10d \times 15d$, the particle spacing $h = 0.052d$ where d is the diameter of the sphere. The spacing of the boundary points is in average the same. The time integrator is Runge Kutta 4 using a time step of $\Delta t = 0.005$. Fig. 7 shows the three-dimensional vorticity structure at $Re = 300$. The surface of the vortices is identified by the λ_2 method of Jeong and Hussain [15]. At $Re = 300$ the flow is unsteady and the vortices shed asymmetrically. This flow behavior matches with the results of Johnson and Patel [17]. The agreement in the flow structure, as well as in the drag and lift coefficients indicates that the present method accurately captures the three-dimensional vorticity field.

4.4 Falling Sphere

The problem of a falling sphere is a simple test case involving fluid-structure interactions. Kern [18] presented this test case to validate the fluid-body coupling procedure. We consider a rigid sphere of density $\rho_s = 1.041 > \rho_0$ at Reynolds

Table 2: Flow past a sphere: Comparison with previous simulations

$Re = 100$	Drag coefficient	Lift coefficient	Strouhal number
pIBM (M =0.1)	1.15	-	-
Fornberg [10]	1.09	-	-
Kim *et al.* FV IBM [19]	1.09	-	-
Fadlun *et al.* [9]	1.08	-	-
$Re = 300$			
pIBM (M =0.1)	0.71	0.062	0.133
Johnson and Patel [16]	0.66	0.069	0.137
Kim *et al.* FV IBM [19]	0.66	0.067	0.134
Ploumhans *et al.* [25]	0.68	0.066	0.137

Table 3: Falling sphere: Convergence study of the falling velocity

Particle spacing h) ($\Delta t = 0.001$)	Falling velocity (t=10)	Time step Δt ($h = 1/16$)	Falling velocity (t=2)
1/8	1.02	0.004	0.602
1/16	0.95	0.002	0.592
1/32	0.93	0.001	0.596
Johnson *et al.* [16]	1.00	0.0005	0.595

number $Re = 100$ and at Mach number of $M = 0.25$. The sphere is released from rest and accelerates until it reaches its asymptotic falling velocity. The sphere diameter d is set to $d = 1$ and the gravity $g = 20$. The size of the domain is set to $6 \times 20 \times 6$, the time integration is Runge Kutta 2nd order with a time step of $\Delta t = 0.001$. Remeshing is applied every time step. An asymptotic falling velocity of $U = 0.95$ is reached at time $t = 10$ using a particle spacing of 1/16. This velocity is in reasonable agreement with the results of Johnson and Patel [16]. Table 4.4 summarizes the results of the falling sphere.

5 Simulation of Anguilliform Swimming

Complex structures interacting with ambient fluids appear in many biological systems. To demonstrate the performance of the pIBM approach, we present the simulation of anguilliform swimming of a self-propelled eel-like body immersed in a viscous fluid. Anguilliform swimmers, such as lamprey, propel themselves by propagating curvature waves backwards along the body. We compare the simulations results with an incompressible finite-volume solution presented by Kern *et al.* [18]. The solution of Kern *et al.* is second order accurate in space and first order accurate in time using an adaptive grid.

5.1 Introduction

The motion of the body is described by the two-dimensional deformation of the mid-line based on the simulations of Carling *et al.* [2]. The lateral displacement of the mid-line $y_s(s,t)$ in a local system is defined as

$$y_s(s,t) = 0.125\frac{s/L + 0.03125}{1.03125}\sin(2\pi(s/L - t/T)) \tag{35}$$

where s is the arc length along the mid-line of the body ($0 \leq s \leq L$), t is the time, T the periodic time.

The three dimensional body of the swimmer is described by spatially varying ellipsoid cross sections. The length of the two half axis $w(s)$ and $h(s)$ are defined as

$$w(s) = \begin{cases} \sqrt{2w_h s - s^2} & 0 \leq s \leq s_b \\ w_h - (w_h - w_t)\left(\frac{s-s_b}{s_t-s_b}\right)^2 & s_b \leq s \leq s_t \\ w_t\frac{L-s}{L-s_t} & s_t \leq s \leq L \end{cases} \tag{36}$$

$$h(s) = b\sqrt{1 - \left(\frac{s-a}{a}\right)^2} \tag{37}$$

where $w_h = s_b = 0.04L$, $s_t = 0.95L$, $w_t = 0.01L$, $a = 0.51L$ and $b = 0.08L$. We apply a no-slip boundary condition on the surface of the body. The mid-line of the body is embedded into a non-inertial (x', y')-system where the center of mass of the deforming body remains and the total angular momentum is conserved. The fluid-body interactions are computed in the inertial system (x,y,z) considering the swimmer as a rigid body. Thus, the motion of the body in the global system (O, x, y, z) is described by the Newtons equations of motion:

$$m\ddot{x}_c = F, \tag{38}$$

$$\dot{I}_z\dot{\varphi}_c + I_z\ddot{\varphi}_c = M_z, \tag{39}$$

where m is the total mass of the immersed body, x_c represents the position of the center of mass, φ_c the global angle with respect to the initial position, F and M_z are the fluid force and yaw torque acting on the body surface. The time-dependency of the inertial moment $\dot{I}_z$ about the yaw axis is also considered although it is small compared to the inertial moment itself.

We set the viscosity of the fluid to be $\mu = 1.4 \cdot 10^{-4}$, the body length $L = 1$, the density $\rho_{0,fluid} = \rho_{body} = \rho = 1$ resulting in a Reynolds number of 3850 based on the final swimming speed.

The fluid forces acting on the body are shown as non-dimensional coefficients $C_\parallel = F_\parallel/(0.5\rho U_0^2 S)$ and $C_\perp = F_\perp/(0.5\rho U_0^2 S)$ parallel and lateral to the swimming direction, where S represents the circumference in two-dimensions and the surface of the body in three dimensions. The yaw torque is measured in the non-dimensional coefficient $C_M = M_z/(0.5\rho U_0^2 LS)$.

5.2 Equations of the Anguilliform Swimmer

The position $\mathbf{x}_c$ and the angle φ_c of anguilliform swimmer evolve by the following set of equations based on Eqs. (38) and (39)

$$\begin{aligned} \frac{d\mathbf{x}_c}{dt} &= \mathbf{u}_c, \\ \frac{d\mathbf{u}_c}{dt} &= \frac{F}{m}, \\ \frac{d\varphi_c}{dt} &= \omega_c, \\ \frac{d\omega_c}{dt} &= \frac{M_z - \dot{I}_z\omega_c}{I_z}, \end{aligned} \tag{40}$$

where u_c denotes the velocity of the swimmer and ω_c the angular velocity. We solve this set of equations simultaneously with the particle equations (Eq. **??**-**??**) that describe the fluid behavior.

5.3 Computational Setup

The particles are initially distributed uniformly in the domain and remeshed every time step. We integrate the Eqns.(**??**)-(**??**), and (40) with respect to time using a explicit 4th order Runge-Kutta scheme with time step of $\Delta t = 0.001$. We consider the domain as an noninertial coordinate system that moves with the opposite x_1-component of the fish velocity such that x_1-position of the fish is constant in the noninertial coordinate system. Thus, we accelerate the fluid in x_1-direction by the opposite force that acts on the swimmer and the swimmer remains on its x_1-position. We impose an inlet and an outlet condition to the boundary ahead and rear of the swimming body, respectively. This approach enables us to reduce the computational effort significantly because our particle solver is currently limited to a uniform resolution. The size of the domain is 4×2 in two dimensions and $3 \times 2 \times 2$ in three dimensions. This domain size is tested to be sufficiently large to neglect the influence of the boundary.

The simulations are based on $1.3{\cdot}10^5$ particles in two dimensions, and $2.5{\cdot}10^7$ particles in three dimensions.

5.4 Results

5.4.1 Two-Dimensional Anguilliform Swimmer

We present a comparison in the two dimensional case with the work of Kern *et al.* [18] in terms of velocity of the swimmer, as well as forces and torque acting on the swimmer. The swimmer accelerates from rest to an asymptotic mean forward velocity of $\bar{U}_{\parallel} = 0.54$ in about seven undulation cycles. The velocity varies slightly during a cycle while the lateral velocity $U_{\perp}$ has an amplitude of 0.04. The time history of the longitudinal and lateral velocity agrees very well with the incompressible solution (Fig. 8). The velocity differs the most at time

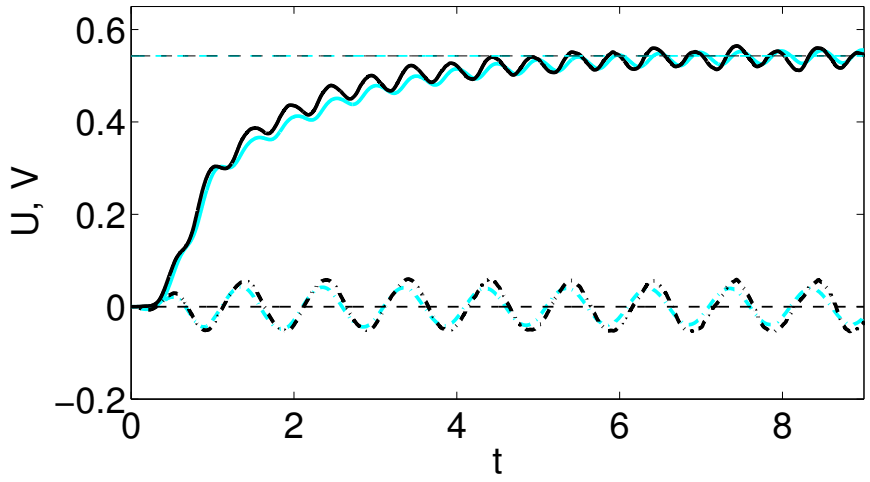

Figure 8: Longitudinal (solid line) and lateral velocity (dashed line) of the two dimensional swimmer compared to finite volume solution (light blue) [18]

$1 < t < 4$ where the density variations are larger than at later time steps. The higher density variations lead to higher pressure variations resulting in larger forces acting on the swimmer. The incompressible solution is approximated sufficiently with a Mach number of $M = 0.1$.

The longitudinal and lateral forces and the torque (Fig. 9) agree very well with the incompressible solution. The force and moment coefficient $C_{\parallel}, C_{\perp}$ and C_M converge to oscillation modes with zero mean and a constant amplitude of 0.03, 0.04 and 0.03, respectively.

Kern *et al.* [18] applied a low pass filter to the fluid force F and the torque M_z to stabilize the simulation of the incompressible flow. We can omit the use of a low pass filter in our study. The compressibility of the fluid causes unresolved pressure waves resulting in high frequent noise in the flow structure. A second order filter [24] is applied to the mass and the momentum during the remeshing process every 100 steps to suppress the small scale pressure waves in the range of the Nyquist frequency. A drawback of the simulation, however, is the remaining noise in the pressure field resulting in noisy forces acting on the swimmer.

Fig. 10 and 11 show the vorticity field of the swimmer during one period at the final swimming speed. The main differences in the vorticity field result from the fact that the particle solution is uniformly resolved, whereas the finite volume solution involves an adaptive re-gridding. Thus, the vorticity shedding at the boundary layer is better resolved in the finite volume solution, the wake pattern behind the tail in the particle solution.

The tail beat amplitude is $A = 0.16$ and the corresponding Strouhal number is $St = 0.59$. The wave velocity is $V = 0.73$, which results in a slip of $\bar{U}_{\parallel}/V =$

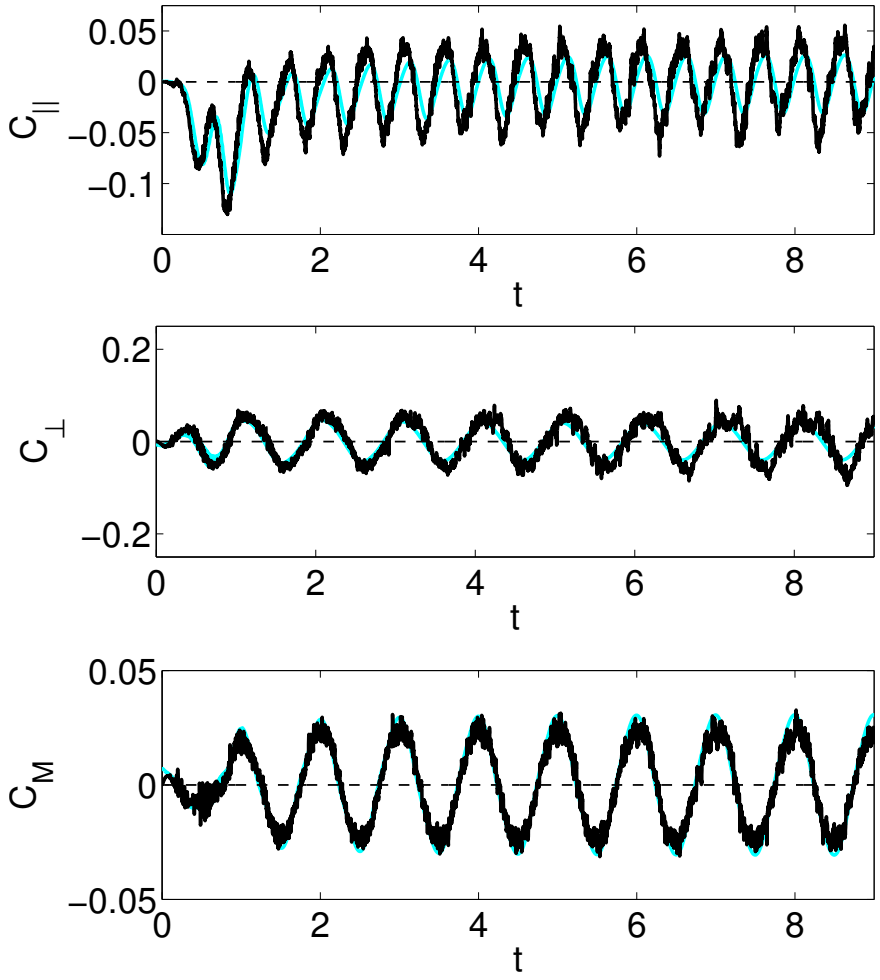

Figure 9: Longitudinal force $C_{\parallel}$, lateral force $C_{\perp}$ and torque C_M of the two dimensional swimmer (black) compared to finite volume solution (light blue) [18]

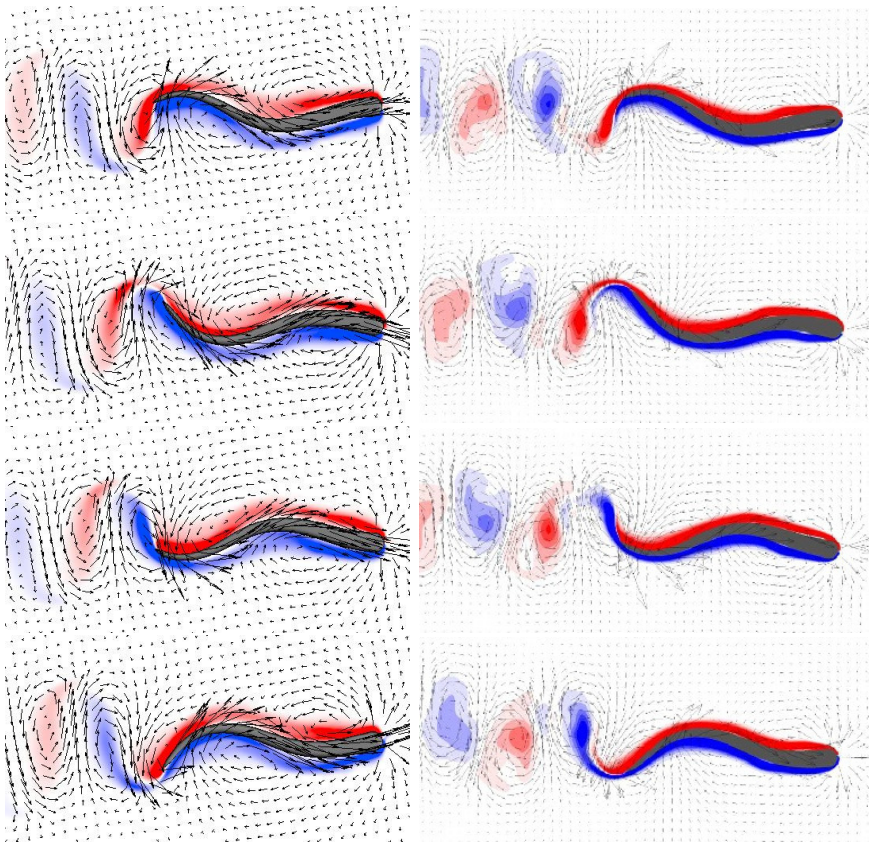

Figure 10: Vorticity field of the two-dimensional swimmer using pIBM (left) and reference solution of Kern [18] (right) for one swmming cycle at time t, t+0.25T, t+0.5T, t+0.75T

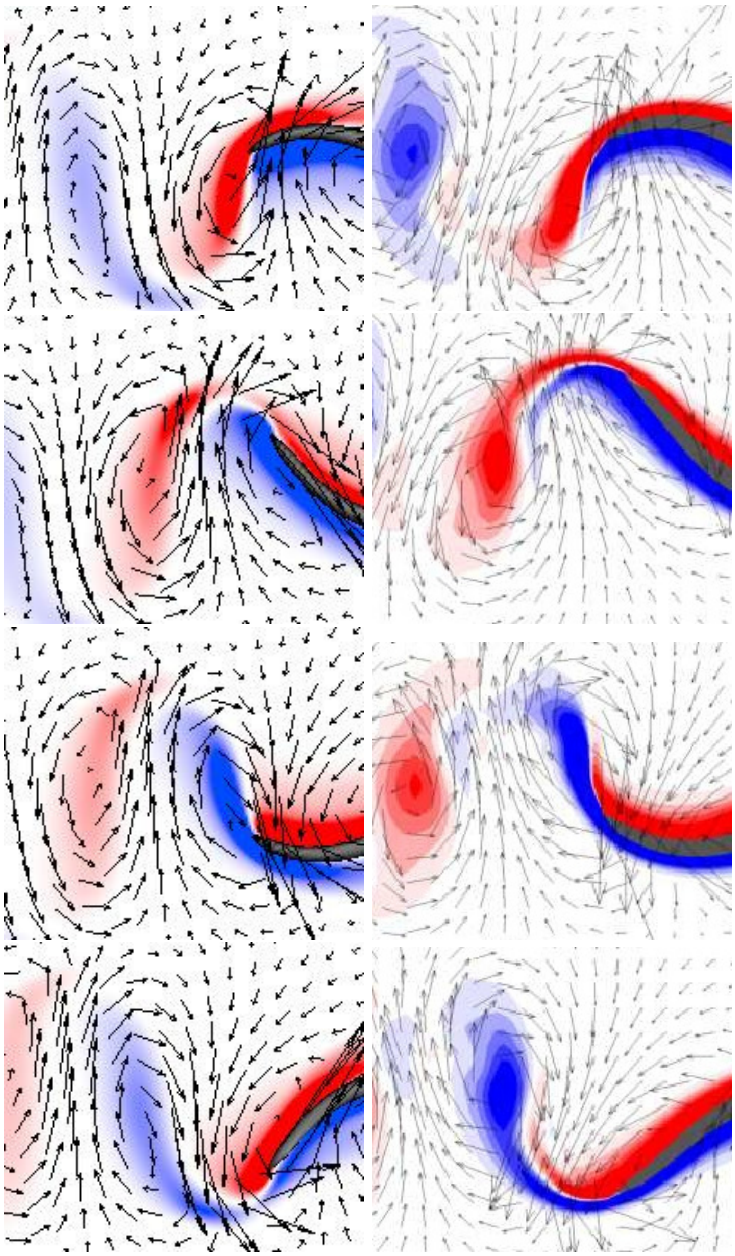

Figure 11: Zoom of the vorticity field at the tail of the two-dimensional swimmer using pIBM (left) and reference solution of Kern [18] (right) for one swmming cycle at time t, t+0.25T, t+0.5T, t+0.75T

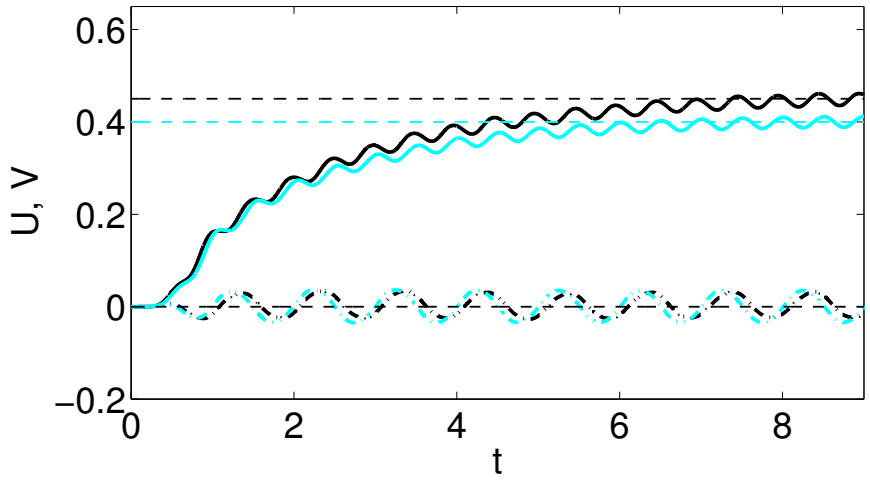

Figure 12: Longitudinal (solid line) and lateral velocity (dashed line) of the three dimensional swimmer compared to finite volume solution (light blue) [18]

0.74.

5.4.2 Three-Dimensional Anguilliform Swimmer

In three dimensions the forces acting on the fish compare well with the finite volume solution (Fig. 13). The net force and moment coefficient $C_{\parallel}, C_{\perp}$ and C_M oscillate with a mean of zero and amplitudes of 0.04, 0.06 and 0.03, respectively. The final swimming speed in the particle solution ($u_{pIBM} = 0.448$) is 12% higher than the result in the finite volume solution ($u_{FV} = 0.402$). This result matches well with the drag comparison in the flow past a sphere at $Re = 300$ where the drag coefficient differs approximately 10% from the results of grid based methods (Table 2). The forward velocity $U_{\parallel}$ oscillates with an amplitude of 0.01. The lateral velocity $U_{\perp}$ has a zero mean and an amplitude of 0.03. The wave velocity $V = 0.73$ is equal to the two dimensional case resulting in the slip of $\bar{U}_{\parallel}/V = 0.61$. The tail beat amplitude is determined to be $A = 0.15$ with $St = 0.67$.

The oscillating tail of the swimmer creates a three-dimensional vortex shedding in the frequency of the swimming motion (Fig. 14-16). Both, the particle and the finite volume solution show the vorticity shed in every half tail beat cycle that breaks up into two vortices forming lateral jets. The vorticity field of particle solution appears smoother and shows less small-scale structures. The vortex rings are less recognizable. As the finite-volume grid feature a four times higher resolution in the boundary layer of the tail than the particle solution, the absence of the small-scale structures in the boundary layer can be associated with a lack of resolution. The small vorticity structures between the shedding

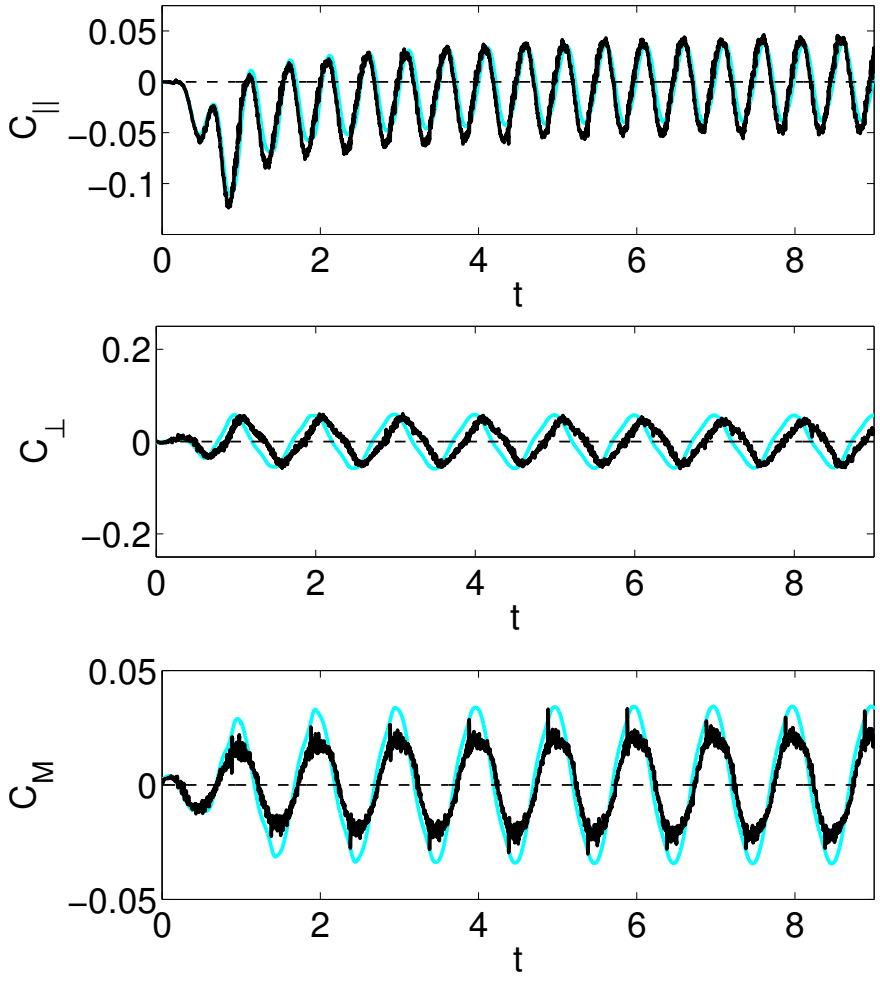

Figure 13: Longitudinal force $C_{\parallel}$, lateral force $C_{\perp}$ and torque C_M of the three dimensional swimmer (black) compared to finite volume solution (light blue) [18]

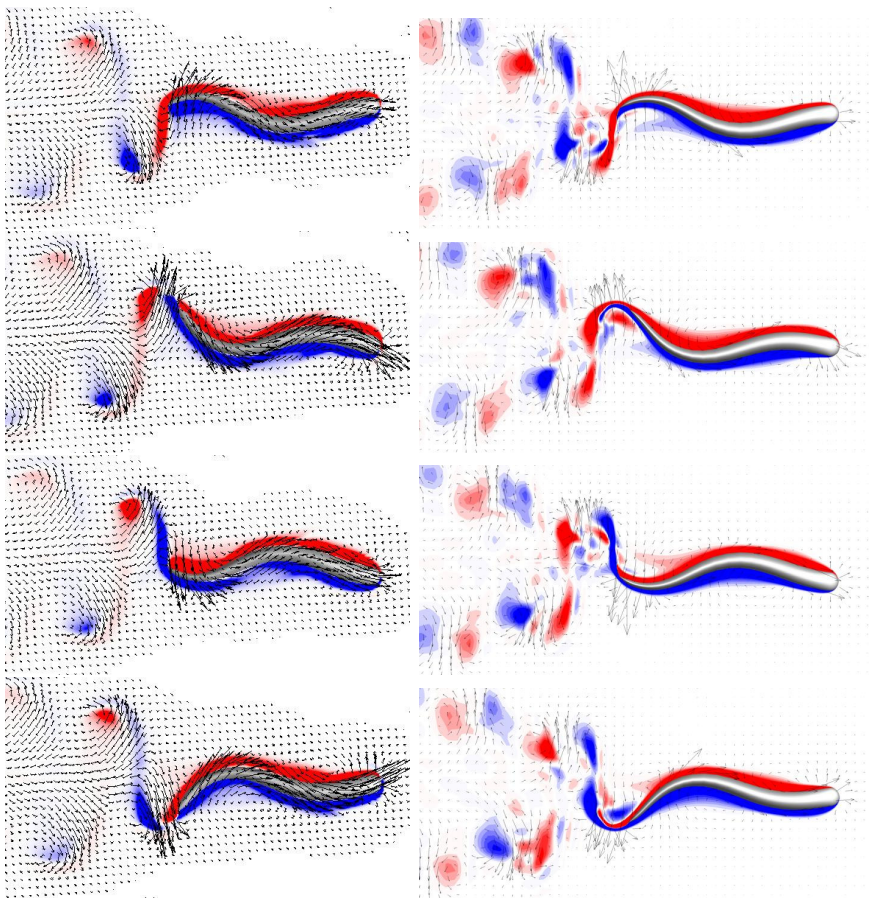

Figure 14: Vorticity field of the three-dimensional swimmer using pIBM (left) and reference solution of Kern [18] (right) for one swmming cycle at time t, t+0.25T, t+0.5T, t+0.75T

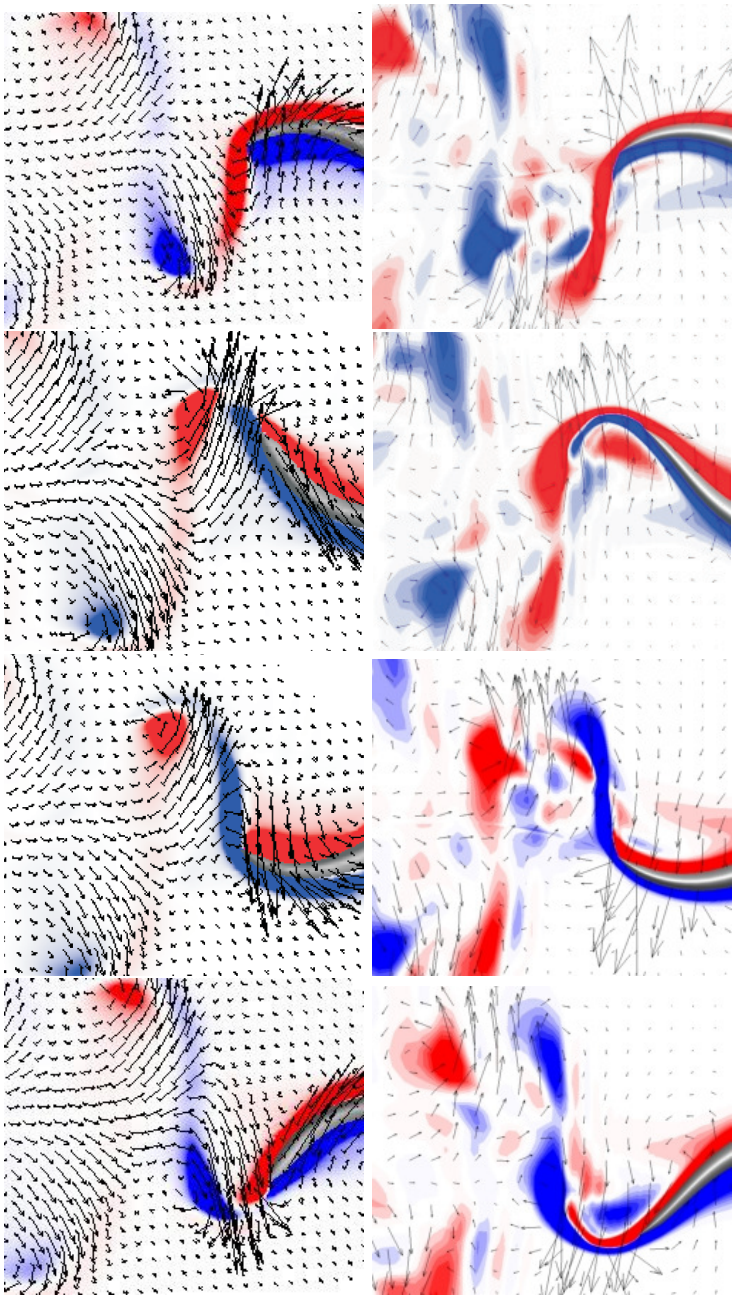

Figure 15: Zoom of the vorticity field at the tail of the three-dimensional swimmer using pIBM (left) and reference solution of Kern [18] (right) for one swmming cycle at time t, t+0.25T, t+0.5T, t+0.75T

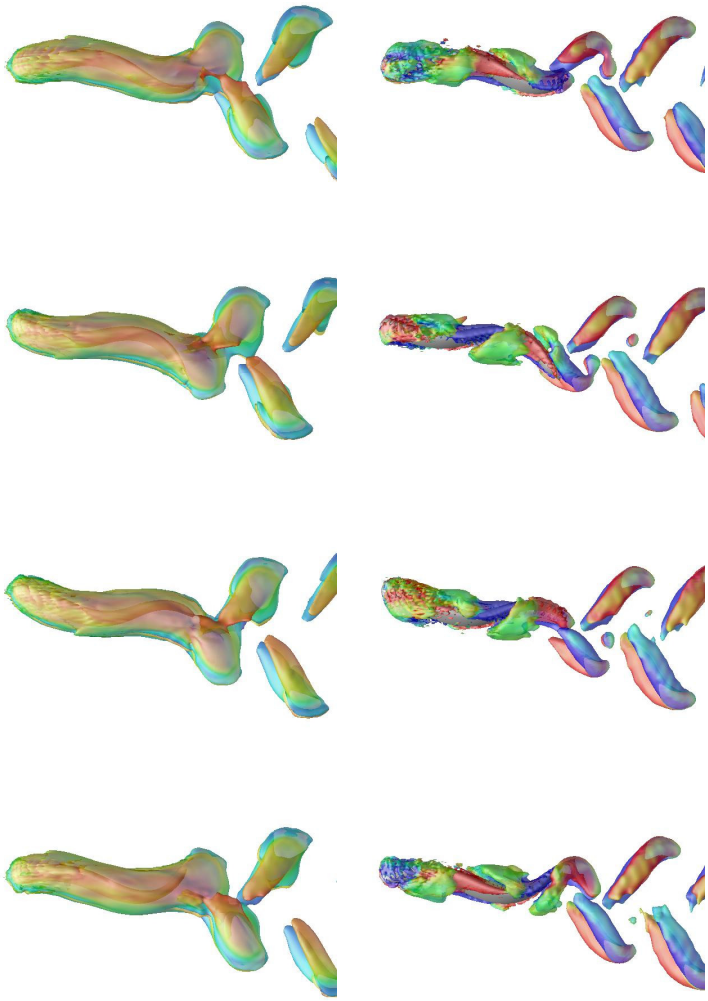

Figure 16: Isosurface of the vorticity magnitude (left) and vortices visualized by the λ_2-method (right) of the three-dimensional swimmer using pIBM for one swmming cycle at time t, t+0.25T, t+0.5T, t+0.75T

vortex pair result are mainly spurious and result from the highly dynamic refinement of the finite volume grid.

Overall, the agreement between the particle and the finite volume solutions is good and shows that the pIBM is appropriate to solve flow-structure interactions accurately.

6 Conclusion

We presented a novel particle Immersed Boundary method for solving the no-slip boundary condition on complex boundaries in two and three dimensions. This method offers accurate flow-structure interaction for particle methods. The method is adaptive as particles adapt to resolve the flow evolution and a consistent remeshing procedure is employed in order to ensure the convergence of the method when the particles get distorted by the flow map. At a Mach Number of 0.1 the simulation agree well with the incompressible solution. The efficiency and accuracy of the method, as well as comparison with related methodologies, is demonstrated in a number of two and three dimensional benchmark problems. The method is shown to be well capable in solving fluid-structure interaction. The simplicity of the method in handling complex boundaries makes it suitable for simulating complex movement of flexible structures as they appear for example in anguilliform swimming. A drawback of this method is the effect of the compressibility of the flow. Fast motions of the boundary in low viscous flow cause pressure waves in the fluid that can lead to numerical problems. Due to pressure waves time step is restricted by the inverse of the speed of sound. Present work involves the embedding of multi-scaling techniques and consideration of further application in the biomedical field of engineering.

7 Acknowledgments

We would like to thank Stefan Kern (ICoS, ETHZ) for several helpful discussions. This project was funded by the Swiss National Science Foundation, NCCR 'Computer Aided and Image Guided Medical Interventions' (Co-Me).

References

[1] J. T. Beale. A convergent 3-D vortex method with grid-free stretching. *Math. Comput.*, 46:401–424, 1986.

[2] John Carling, Thelma L. Williams, and Graham Bowtell. Self-propelled anguilliform swimming: simultaneous solution of the two-dimensional Navier-Stokes equations and Newtons' laws of motion. *J. Exp. Biol.*, 201:3143–3166, 1998.

[3] A. J. Chorin. Numerical study of slightly viscous flow. *J. Fluid Mech.*, 57(4):785–796, 1973.

[4] G.-H. Cottet. Artificial viscosity models for vortex and particle methods. *J. Comput. Phys.*, 127:299–308, 1996.

[5] G.-H. Cottet and P. Koumoutsakos. *Vortex Methods – Theory and Practice.* Cambridge University Press, New York, 2000.

[6] Georges-Henri Cottet, Bertrand Michaux, Sepand Ossia, and Geoffroy VanderLinden. A comparison of spectral and vortex methods in three-dimensional incompressible flows. *J. Comput. Phys.*, 175:702–712, 2002.

[7] P. Degond and S. Mas-Gallic. The weighted particle method for convection-diffusion equations. part 1: The case of an isotropic viscosity. *Math. Comput.*, 53(188):485–507, 1989. Oct.

[8] Jeff D. Eldredge, Anthony Leonard, and Tim Colonius. A general deterministic treatment of derivatives in particle methods. *J. Comput. Phys.*, 180(2):686–709, 2002.

[9] E. A. Fadlun, R. Verzicco, P. Orlandi, and J. Mohd-Yusof. Combined immersed-boundary finite-difference methods for three-dimensional complex flow simulations. *J. Comput. Phys.*, 161(1):35–60, 2000.

[10] Bengt Fornberg. Steady viscous flow past a sphere at high Reynolds numbers. *J. Fluid Mech.*, 190:471–489, 1988.

[11] Ole H. Hald. Convergence of vortex methods for Euler's equations, III. *SIAM J. Numer. Anal.*, 24(3):538–582, 1987.

[12] R. D. Henderson. Details of the drag curve near the onset of vortex shedding. *Phys. Fluids*, 7:2102–2104, 1995.

[13] S. E. Hieber, J. H. Walther, and P. Koumoutsakos. Remeshed smoothed particle hydrodynamics simulation of the mechanical behavior of human organs. *J. Technology and Health Care*, 12(4):305–314, 2004.

[14] Simone Elke Hieber and Petros Koumoutsakos. A Lagrangian particle level set method. *J. Comput. Phys.*, 210:342–367, 2005.

[15] H. Jeong, B. Tombor, R. Albert, Z. N. Oltvai, and A.-L. Barabási. The large-scale organization of metabolic networks. *Nature*, 407:651–654, 2000.

[16] A. T. Johnson and V. C. Patel. Flow past a sphere up to a Reynolds number of 300. *J. Fluid Mech.*, 378:19–70, 1999.

[17] Gordon R. Johnson, Robert A. Stryk, and Stephen R. Beissel. SPH for high velocity impact computations. *Comp. Meth. Appl. Mech. & Engng.*, 139:347–373, 1996.

[18] Stefan Kern and Petros Koumoutsakos. Simulations of optimized anguilliform swimming. *J. Exp. Biol.*, page submitted, 2006.

[19] Jungwoo Kim, Dongjoo Kim, and Haecheon Choi. An immersed-boundary finite-volume method for simulations of flow in complex geometries. *J. Comput. Phys.*, 171:132–150, 2001.

[20] P. Koumoutsakos. Vorticity flux control in a turbulent channel flow. *Phys. Fluids*, 11(2):248–250, 1999.

[21] J. J. Monaghan. Smoothed particle hydrodynamics. *Annu. Rev. Astron. Astrophys.*, 30:543–574, 1992.

[22] J. Park, K. Kwon, and H. Choi. Numerical solutions of flow past a cylinder at Reynolds number up to 160. *KSME Int. J.*, 12(6):1200–1205, 1998.

[23] Charles Peskin. Flow patterns around heart valves: A numerical study. *J. Comput. Phys.*, 10:252–271, 1972.

[24] Roger Peyret and Thomas Taylor. *Computational Methods for Fluid Flow.* Springer-Verlag, 1983.

[25] P. Ploumhans, G. S. Winckelmans, J. K. Salmon, A. Leonard, and M. S. Warren. Vortex methods for direct numerical simulation of three-dimensional bluff body flows: Applications to the sphere at $Re = 300$, 500 and 1000. *J. Comput. Phys.*, 178:427–463, 2002.

[26] Anatol Roshko. Experiments on the flow past a circular cylinder at very high Reynolds number. *J. Fluid Mech.*, 10(3):345–356, 1961.

[27] I. F. Sbalzarini, J. H. Walther, M. Bergdorf, S. E. Hieber, E. M. Kotsalis, and P. Koumoutsakos. PPM – a highly efficient parallel particle-mesh library for the simulation of continuum systems. *J. Comput. Phys.*, 215:566–588, 2006.

[28] A. L. F. Silva, A. Silveira-Neto, and J. J. R. Damasceno. Numerical simulations of two-dimensional flows over a circular cylinder using the immersed boundary method. *J. Comput. Phys.*, 189:351–370, 2003.

[29] S. P. Singh and S. Mittal. Flow past a cylinder: shear layer instability and drag crisis. *J. Comput. Phys.*, 47:75–98, 2005.

[30] C. H. K. Williamson. Oblique and parallel modes of vortex shedding in the wake of a circular cylinder at low Reynolds numbers. *J. Fluid Mech.*, 206:579–627, 1989.